HAL
open science

Numerical modeling of shallow non-Newtonian flows: Part I. The 1D horizontal dam break problem revisited

Pierre Saramito, Claude Smutek, Benoit Cordonnier

To cite this version:

Pierre Saramito, Claude Smutek, Benoit Cordonnier. Numerical modeling of shallow non-Newtonian flows: Part I. The 1D horizontal dam break problem revisited. International Journal of Numerical Analysis & Modeling, Series B, 2013, 4 (3), pp.283-298. hal-00463791v4

HAL Id: hal-00463791

https://hal.science/hal-00463791v4

Submitted on 5 Sep 2013

HAL is a multi-disciplinary open access archive for the deposit and dissemination of scientific research documents, whether they are published or not. The documents may come from teaching and research institutions in France or abroad, or from public or private research centers.

L'archive ouverte pluridisciplinaire **HAL**, est destinée au dépôt et à la diffusion de documents scientifiques de niveau recherche, publiés ou non, émanant des établissements d'enseignement et de recherche français ou étrangers, des laboratoires publics ou privés.

INTERNATIONAL JOURNAL OF
NUMERICAL ANALYSIS AND MODELING, *SERIES B*
Volume 1, Number 1, Pages 1–18

© 2013 Institute for Scientific
Computing and Information

NUMERICAL MODELING OF SHALLOW NON-NEWTONIAN FLOWS: PART I. THE 1D HORIZONTAL DAM BREAK PROBLEM REVISITED

PIERRE SARAMITO[1], CLAUDE SMUTEK[2], AND BENOÎT CORDONNIER[2,3]

(Communicated by Yanping Lin)

Abstract. The dam break problem shallow approximation for laminar flows of power-law non-Newtonian fluids is numerically revisited under a time and space second order adaptive method. Theoretical solutions are compared with experimental measurements from the literature and new ones made of silicon. Asymptotic behaviours are solved numerically and from autosimilar solutions. The obtained theoretical results are finally compared with experiments. These comparisons confirm the validity of the shallow approximation equations for non-Newtonian fluids subject to the horizontal dam break problem.

Key words. fluid mechanics ; non-Newtonian fluid ; power-law model ; asymptotic analysis ; shallow water theory

1. Introduction

Barré de Saint-Venant [27] developed in 1887 the firsts shallow water theory for fast Newtonian flows: the flow was driven by inertia terms while viscous effects were neglected. This study was first motivated by hydraulic engineering applications. More recently slower Newtonian flows [19] and the effect of viscous terms [13] were investigated. Both the manufacturing processes (concretes, foods) and the environmental applications (e.g. mud flows [11, 20], volcanic lava [14], dense snow avalanches [2] or submarine landslides [15]) require more complex non-Newtonian rheologies. For these rheologies, shallow approximations were first studied for a viscoplastic fluid by Lui and Mei [21] and revisited by Balmforth and Craster [6]. See [8, 3] for recent reviews on this subject. The dam break problem in a horizontal channel is a standard problem of fluid mechanics which finds applications in numerous environmental or industrial processes that is used as a standard benchmark for evaluating the shallow water approximations. One may also note the recent interest in a similar benchmark, the Bostwick consistometer, used in food industry [23, 22, 24, 7]. Despite these numerous applications and theoretical development, only few experimental measurements are available for the elemental case of the horizontal dam break problem. The Newtonian case has been investigated with glucose in [26] while the non-Newtonian one was discussed in [7] for power-law fluids. Furthermore, the nonlinear reduced equation obtained by the asymptotic method in the shallow limit does not admit an explicit solution and composite [18] or autosimilar solutions [17, 25, 5] were proposed instead (see also [4]). Thus, all available works are based on some simplifications and a direct numerical resolution without any simplification is of the utmost interest to fully solve this nonlinear problem, especially its long-time behaviour.

Received by the editors October 6, 2012 and, in revised form, June 25, 2013.
2000 *Mathematics Subject Classification.* 35K65, 65M50, 65M60, 76A05.

The aim of this paper is to bring a new robust and efficient numerical method for the resolution of the shallow approximation of the dam break problem and beyond, adjoin some new experimental measurements to the non-Newtonian power-law case. The present numerical scheme provides a fully automatic space-adaptive feature which enables an accurate capture of the front position and also is able to predict accurately the long-time behaviour of the model. Moreover, the proposed adaptive algorithm naturally extends to both viscoplastic flows and shallow approximations of three-dimensional free surface flows. The problem is solved for various power law indexes and a general front propagation rule $x_f(t)$ is proposed for any power-law index n.

This manuscript has been divided as follow: Section 2 introduces the dam break problem statement and section 3 the reduced problem obtained after the asymptotic analysis under the shallow flow approximation. Section 4 develops details of the numerical resolution of this nonlinear problem. Section 5 presents the numerical results and finally, section 6 develops the experimental measurements and the comparison between theory and experiments for the presents results and previous measurements available in the literature.

2. Problem statement

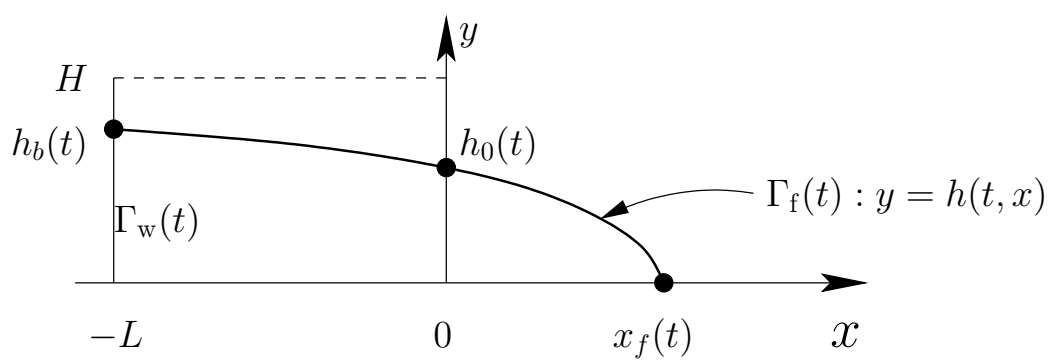

FIGURE 1. Schematic view of the dam break problem.

The classical bidimensional dam break problem for a quasi-Newtonian power-law fluid model is considered. It leads to the following problem:
find the velocity field $\mathbf{u}$ and the pressure field p, defined for all time $t > 0$ and in the time-dependent domain $\Omega(t)$, such that:

$$\rho\left(\frac{\partial \mathbf{u}}{\partial t} + \mathbf{u}.\nabla\mathbf{u}\right) - \mathbf{div}\left(2\kappa\left|D(\mathbf{u})\right|^{n-1} D(\mathbf{u})\right) + \nabla p = \rho\mathbf{g} \quad \text{in }]0,+\infty[\times\Omega(t), \tag{1a}$$

$$\operatorname{div}\mathbf{u} = 0 \quad \text{in }]0,+\infty[\times\Omega(t), \tag{1b}$$

$$\mathbf{u}(t=0) = 0 \quad \text{in } \Omega(0), \tag{1c}$$

$$\mathbf{u} = 0 \quad \text{on }]0,+\infty[\times\Gamma_{\rm w}(t), \tag{1d}$$

$$\sigma.\mathbf{n} = 0 \quad \text{on }]0,+\infty[\times\Gamma_{\rm f}(t), \tag{1e}$$

where ρ is the density constant, κ the consistency constant, $n > 0$ the power-law index and $\mathbf{g}$ the gravity force vector. When $n = 1$, the fluid is Newtonian, with the classical Navier-Stokes equations. The shear thinning behaviour is associated with $0 < n < 1$ and the shear thickening behaviour to $n > 1$. The notation $|D(\mathbf{u})|$

denotes the second invariant of the rate of deformation tensor $D(\mathbf{u}) = (\nabla\mathbf{u} + \nabla\mathbf{u}^T)/2$. Here, (1a) and (1b) are respectively the momentum and mass conservation equations for an isochoric fluid. These equations are completed with the appropriate initial and boundary conditions: an initial condition for the velocity (1c), adhesion at the wall of the reservoir (1d), and equilibrium at the free surface (1e), where surface tension is neglected. Here, $\sigma = -p.I + 2\kappa\,|D(\mathbf{u})|^{n-1}\,D(\mathbf{u})$ is the total stress tensor. The pressure outside the free surface is supposed to be constant (i.e. the atmospheric pressure). Since the pressure is defined here up to a constant, we can conveniently define the atmospheric pressure as zero. The fluid domain and the free surface are respectively defined for all time $t \geq 0$ by

$$\begin{aligned}\Omega(t) &= \{(x,y) \in\,]-L,+\infty[\times]0,H[;\ \phi(t,x,y) < 0\},\\ \Gamma_{\mathrm{f}}(t) &= \{(x,y) \in\,]-L,+\infty[\times]0,H[;\ \phi(t,x,y) = 0\},\end{aligned}$$

where $\phi(t,x,y) = y - h(t,x)$ is the indicator function of the flow domain, and $h(t,x)$ is the flow height for a given time t and position x (see Fig. 1). The wall part of the flow domain boundary is $\Gamma_{\mathrm{f}}(t) = \partial\Omega(t) - \Gamma_{\mathrm{f}}(t)$. The flow domain is transported by the velocity: $\dfrac{\partial\phi}{\partial t} + \mathbf{u}.\nabla\phi = 0$ which may equivalently be written:

$$\frac{\partial h}{\partial t}(t,x) + u_x(t,x,h(t,x))\,\frac{\partial h}{\partial x}(t,x) = u_y(t,x,h(t,x)), \quad \forall (t,x) \in]0,+\infty[\times]0;+\infty[, \tag{1f}$$

where $\mathbf{u} = (u_x, u_y)$. This equation is completed with the initial condition

$$h(t{=}0,x) = \begin{cases} H & \text{when } -L < x < 0,\\ 0 & \text{when } x > 0.\end{cases} \tag{1g}$$

3. The reduced problem

In the context of Bingham [9] fluids, Liu and Mei [21] proposed an asymptotic analysis for slow flows and small H/L ratio. Revisited in [6], this analysis has also been extended to an Herschel-Bulkley [16] fluid or a fluid with a power-law index n (see also [7]). For a fluid with a power-law index, the height $h(t,x)$ is the single remaining unknown of the reduced problem:
(P): find h, defined in $]0,+\infty[\times]-L,+\infty[$, such that

$$\frac{\partial h}{\partial t} - \left(\frac{\rho g}{K}\right)^{\frac{1}{n}} \frac{\partial}{\partial x}\left(q_n\left(h, \frac{\partial h}{\partial x}\right)\right) = 0 \quad \text{in }]0,+\infty[\times]-L,+\infty[\tag{2a}$$

$$\frac{\partial h}{\partial x}(t,-L) = \frac{\partial h}{\partial x}(t,+\infty) = 0, \quad \forall t \in]0,+\infty[\tag{2b}$$

$$h(0,x) = \begin{cases} H & \text{when } x < 0\\ 0 & \text{otherwise}\end{cases} \tag{2c}$$

where, for all $\xi \geq 0$ and $\zeta \in \mathbb{R}$:

$$q_n(\xi,\zeta) = \begin{cases} 0, & \text{when } \zeta = 0,\\ \frac{n}{2n+1}\xi^{2+\frac{1}{n}}|\zeta|^{\frac{1}{n}}\mathrm{sgn}(\zeta), & \text{otherwise}\end{cases}$$

Problem (2) is a highly nonlinear degenerate parabolic problem similar to the so-called p-Laplacian problem (with $p = 1 + 1/n$). Its numerical resolution requires some care, as the flux q_n vanishes when either h or $\partial h/\partial x$ vanish. We introduce the dimensionless quantities:

$$\hat{h} = \frac{h}{H}, \quad \hat{x} = \frac{x}{L}, \quad \hat{t} = \frac{t}{T}$$

where

$$T = \frac{L}{H}\left(\frac{KL}{\rho g H^2}\right)^{\frac{1}{n}}$$

Then, the dimensionless reduced problem becomes:
$(\hat{P})$: find $\hat{h}$, defined in $]0,+\infty[\times]-1,+\infty[$, such that

$$\frac{\partial \hat{h}}{\partial \hat{t}} - \frac{\partial}{\partial \hat{x}}\left(q_n\left(\hat{h}, \frac{\partial \hat{h}}{\partial \hat{x}}\right)\right) = 0 \quad \text{in }]0,+\infty[\times]-1,+\infty[\tag{3a}$$

$$\frac{\partial \hat{h}}{\partial \hat{x}}(\hat{t},-1) = \frac{\partial \hat{h}}{\partial \hat{x}}(\hat{t},+\infty) = 0, \quad \forall \hat{t} \in]0,+\infty[\tag{3b}$$

$$\hat{h}(0,\hat{x}) = \begin{cases} 1 & \text{when } \hat{x} < 0 \\ 0 & \text{otherwise} \end{cases} \tag{3c}$$

This is a parabolic nonlinear problem, with only n as a parameter. One may observe that this problem does not reduces to the usual shallow water model introduced by Barré de Saint-Venant [27] for turbulent flows. From our analysis the viscous term is not neglected but the inertia one is removed during the asymptotic analysis.

4. Numerical resolution

This section focuses on time and space approximations of the reduced problem. A semi-implicit time approximation scheme is first presented, and improved by a fixed-point internal loop. Each step requires the resolution of a linear second-order elliptic sub-problem.

4.1. Time approximation and algorithms. Notice that the initial condition $h_0(x)$ is discontinuous. The diffusive term smears out this initial discontinuity instantaneously when the fluid starts to slump and the solution of the parabolic problem presents a sharp transition at the vicinity of $t = 0$. For that reason, we opt for a second order fully implicit and variable time step algorithm. The time step is set small at the vicinity of $t = 0$ and increases with a geometric progression. Let $(t_m)_{m\geq 0}$ denotes the time discretization sequence and $\Delta t_m = t_{m+1} - t_m$, $m \geq 0$ be the time step. The first-order time derivative is approximated by the following second-order finite difference scheme, defined for all function $\varphi \in C^0$ by:

$$\begin{aligned}\frac{\partial \varphi}{\partial t}(t_{m+1}) &= \frac{2\Delta t_m + \Delta t_{m-1}}{\Delta t_m(\Delta t_m + \Delta t_{m-1})}\varphi(t_{m+1}) - \frac{\Delta t_m + \Delta t_{m-1}}{\Delta t_m \Delta t_{m-1}}\varphi(t_m) \\ &\quad + \frac{\Delta t_m}{(\Delta t_m + \Delta t_{m-1})\Delta t_{m-1}}\varphi(t_{m-1}) + \mathcal{O}(\Delta t_m^2 + \Delta t_{m-1}^2)\end{aligned}$$

We introduce $(\hat{h}^m)_{m\geq 0}$ with $\hat{h}^m(\hat{x}) \approx \hat{h}(m\Delta\hat{t},\hat{x})$ recursively defined by the following algorithm:

ALGORITHM 1

- $m = -1, 0$: $\hat{h}^0 := \hat{h}^{-1} := \hat{h}(\hat{t} = 0)$

- $m \geq 1$: given $\hat{h}^{m-1}$ and $\hat{h}^{m}$, find $\hat{h}^{m+1}$ such that:

$$\frac{2\Delta t_m + \Delta t_{m-1}}{\Delta t_m(\Delta t_m + \Delta t_{m-1})}\hat{h}^{m+1} - \frac{\mathrm{d}}{\mathrm{d}\hat{x}}\left(\nu_n\left(\hat{h}^{m+1}, \frac{\mathrm{d}\hat{h}^{m+1}}{\mathrm{d}\hat{x}}\right)\frac{\mathrm{d}\hat{h}^{m+1}}{\mathrm{d}\hat{x}}\right)$$

$$= \frac{\Delta t_m + \Delta t_{m-1}}{\Delta t_m \Delta t_{m-1}}\hat{h}^{m} - \frac{\Delta t_m}{(\Delta t_m + \Delta t_{m-1})\Delta t_{m-1}}\hat{h}^{m-1} \quad \text{in }]-1,+\infty[\tag{4a}$$

$$\frac{\mathrm{d}\hat{h}^{m+1}}{\mathrm{d}\hat{x}}(-1) = \frac{\mathrm{d}\hat{h}^{m+1}}{\mathrm{d}\hat{x}}(+\infty) = 0 \tag{4b}$$

where, for all $\xi \geq 0$ and $\zeta \in \mathbb{R}$:

$$\nu_n(\xi,\zeta) = \begin{cases} 0, & \text{when } \zeta = 0, \\ \frac{n}{2n+1}\xi^{2+\frac{1}{n}}|\zeta|^{-1+\frac{1}{n}}\mathrm{sgn}(\zeta), & \text{otherwise} \end{cases}$$

Algorithm 1 corresponds to an implicit second-order backward discretization scheme with variable time step. This scheme is used for all the computations undertaken in the next sections. The initial time-dependent problem is transformed to a sequence of nonlinear sub-problems (4a)-(4b), since, at each iteration m, $\hat{h}^{m+1}$ is unknown. The simplest idea is to solve each sub-problem by using an inner fixed-point loop:

ALGORITHM 2.a

- $k = 0$: $\varphi^0 := \hat{h}^m$
- $k \geq 1$: given φ^k, find φ^{k+1} such that:

$$\begin{aligned} \alpha_m\varphi^{k+1} - \frac{\mathrm{d}}{\mathrm{d}\hat{x}}\left(\nu_n\left(\varphi^k, \frac{\mathrm{d}\varphi^k}{\mathrm{d}\hat{x}}\right)\frac{\mathrm{d}\varphi^{k+1}}{\mathrm{d}\hat{x}}\right) &= f_m \quad \text{in }]-1,+\infty[\\ \frac{\mathrm{d}\varphi^{k+1}}{\mathrm{d}\hat{x}}(-1) = \frac{\mathrm{d}\varphi^{k+1}}{\mathrm{d}\hat{x}}(+\infty) &= 0 \end{aligned}$$

where

$$\begin{aligned} \alpha_m &= \frac{2\Delta t_m + \Delta t_{m-1}}{\Delta t_m(\Delta t_m + \Delta t_{m-1})} \\ f_m &= \frac{\Delta t_m + \Delta t_{m-1}}{\Delta t_m \Delta t_{m-1}}\hat{h}^{m} - \frac{\Delta t_m}{(\Delta t_m + \Delta t_{m-1})\Delta t_{m-1}}\hat{h}^{m-1} \end{aligned}$$

Algorithm 2.a reduces to an elliptic second order differential equation with non-constant coefficients. The k loop stops for a residual term lower than a given tolerance $\varepsilon > 0$. Then, we set $\hat{h}^{m+1} := \varphi^k$. Notice that there are two imbricated loops here: an outer one, the m loop, associated to the time discretisation, and a inner one, the k loop, associated to the fixed point algorithm. At convergence of the inner loop, subproblem (4) is fully solved and thus, the scheme is a fully implicit second order one.

In practice, we observe that this algorithm converges only for $n \in]1/2, 2[$ and poorly converge for large meshes. Thus, in order to solve the nonlinear sub-problem (4a)-(4b), we defined a more robust algorithm:

ALGORITHM 2.b

- $k = 0$: $\varphi^0 := \hat{h}^m$
- $k \geq 1$: given φ^k, find φ^{k+1} such that:

$$\alpha_m\varphi^{k+1} - \frac{\mathrm{d}}{\mathrm{d}\hat{x}}\left(\mu_n\left(\varphi^k\right)\left|\frac{\mathrm{d}\varphi^{k+1}}{\mathrm{d}\hat{x}}\right|^{\frac{1}{n}}\right) = f_m \quad \text{in }]-1,+\infty[\tag{5a}$$

$$\frac{\mathrm{d}\varphi^{k+1}}{\mathrm{d}\hat{x}}(-1) = \frac{\mathrm{d}\varphi^{k+1}}{\mathrm{d}\hat{x}}(+\infty) = 0 \tag{5b}$$

where, for all $\xi \geq 0$:

$$\mu_n(\xi) = \frac{n}{2n+1}\xi^{2+\frac{1}{n}}$$

For a fixed iteration $k \geq 0$, observe that the sub-problem (5a)-(5b) is still nonlinear. This is the so-called p-Laplacian problem, with $p = 1 + 1/n > 1$. Let $L^p(-1,+\infty)$ and $W^{1,p}(-1,+\infty)$ denote the usual Sobolev functional spaces [1]. Observe that the solution of (5a)-(5b) is characterised as the minimum of the following energy-like function, defined for all $\varphi \in W^{1,p}(-1,+\infty)$ by:

$$J_{k,m}(h) = \frac{\alpha_m}{2}\int_{-1}^{+\infty} \varphi^2 \,\mathrm{d}x + \frac{n}{n+1}\int_{-1}^{+\infty} \mu_n(\varphi_k)|\varphi'|^{1+\frac{1}{n}} \,\mathrm{d}x - \int_{-1}^{+\infty} f_m \hat{h} \,\mathrm{d}x$$

Following [12, p. 128], we consider the quantity $\delta = \varphi' \in L^p(-1,+\infty)$ as an independent variable. The constraint $\delta - \varphi' = 0$ is enforced by using a Lagrange multiplier $\tau \in L^{p'}(-1,+\infty)$, where $p' = 1 - 1/p = 1/(1+n)$. The following augmented Lagrangian is then introduced by:

$$\begin{aligned} L_{k,m}((\varphi,\delta);\tau) \quad = \quad & \frac{\alpha_m}{2}\int_{-1}^{x_e} \varphi^2 \,\mathrm{d}x + \frac{n}{n+1}\int_{-1}^{x_e} \mu_n(\varphi_k)|\delta|^{1+\frac{1}{n}} \,\mathrm{d}x - \int_{-1}^{x_e} f_m\,\varphi \,\mathrm{d}x \\ & + \int_{-1}^{x_e} (\varphi' - \delta)\,\tau \,\mathrm{d}x + \frac{\beta}{2}\int_{-1}^{x_e} |\varphi' - \delta|^2 \,\mathrm{d}x \end{aligned}$$

where $\beta > 0$ is the augmentation parameter of the Lagrangian. The previous minimisation problem is equivalent to a saddle point problem:

$$\inf_{(\varphi,\delta)\in W^{1,p}\times L^p} \quad \sup_{\tau\in L^{p'}} L_{m,k}((\varphi,\delta);\tau)$$

The solution is independent of β since the solution of the saddle point problem satisfies $\delta = \varphi'$. An Uzawa minimisation algorithm for finding the saddle point of $L_{m,k}$ is written:

ALGORITHM 3

- $l = 0$: let δ_0 and τ_0 arbitrarily chosen.
- $l \geq 0$: let δ_l and τ_l being known, find φ_{l+1} such that

$$\left\{ \begin{array}{rcl} \alpha\varphi_{l+1} - \beta\varphi''_{l+1} & = & f - (\tau_l - \beta\delta_l) \ \text{ in }]-1, x_e[\\ \varphi'_{l+1}(-1) = \varphi'_{l+1}(+\infty) & = & 0 \end{array} \right. \tag{6}$$

then, we compute δ_{l+1} in a point-by-point way:

$$\delta_{l+1}(x) = \Phi_{n,\beta}\left(\mu_n(\varphi_k(x)),\, \tau_l(x) + \beta\varphi'_{l+1}(x)\right) \tag{7}$$

and finally, we compute explicitly τ_{l+1} as:

$$\tau_{l+1} = \tau_l + \beta(\varphi'_{l+1} - \delta_{l+1}) \tag{8}$$

Problem (6) is linear and standard which yields to a really fast solution especially in one space dimension. The nonlinearity of the problem is treated in (7) where the function $\Phi_{n,\beta}$ is defined for all $\bar{\mu}, \zeta \in \mathbb{R}$ by:

$$\Phi_{n,\beta}(\bar{\mu},\,\zeta) = \arg\min_{\delta\in\mathbb{R}} \frac{\bar{\mu}\,n}{n+1}|\delta|^{1+\frac{1}{n}} + \frac{\beta}{2}\delta^2 - \zeta\,\delta$$

Since this minimisation problem in $\mathbb{R}$ is convex, its solution $\delta \in \mathbb{R}$ is unique and then $\Phi_{n,\beta}$ is well defined. The minimisation problem is also differentiable and its solution satisfies $\bar{\mu}|\delta|^{\frac{1}{n}}\mathrm{sgn}(\delta) + \beta\delta - \zeta = 0$ where sgn denotes the sign function. Note that when $n = 1$, i.e. the Newtonian model, the computation is explicit: $\delta = \zeta/(\bar{\mu} + \beta)$. In the general case of the power-law model, when $n > 0$, we consider the Newton algorithm:

- $q = 0$: let δ_0 given.
- $q \geq 0$: let δ_q being known and compute

$$\delta_{q+1} = \delta_q - \frac{\bar{\mu}|\delta_q|^{\frac{1}{n}}\mathrm{sgn}(\delta_q) + \beta\delta_q - \zeta}{\frac{1}{n}\bar{\mu}|\delta_q|^{\frac{1}{n}-1} + \beta}$$

In practice, the Newton algorithm is initialised with $\delta_0 = \zeta/(\bar{\mu}+\beta)$ and we observe that the convergence is very fast. Also, algorithms 2.b and 3 are combined in a flatten algorithm, where only one iteration of the l inner loop is performed. This leads to an efficient and robust strategy for the numerical resolution of the nonlinear problem.

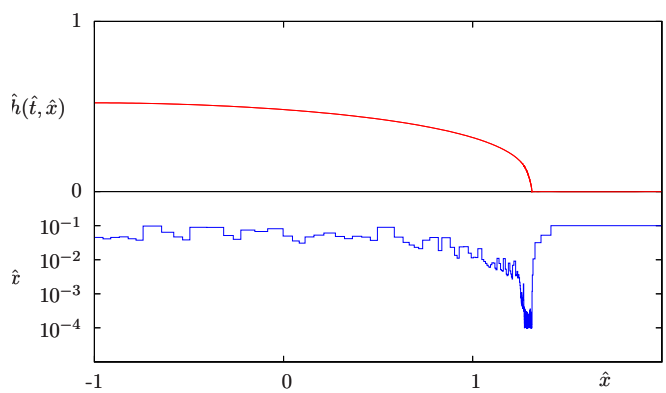

FIGURE 2. Adaptive subdivision for the dam break problem $n = 0.9$, $t = 15$: 1145 elements.

4.2. Space approximation and adaptive subdivision. The problem is discretized with respect to the space variable $\hat{x}$ by a quadratic finite element method in a bounded interval $]-1, \hat{x}_e[$, where $\hat{x}_e$ is chosen sufficiently large. The matrix of the subproblems involves a bandwidth equal to five and the linear system can efficiently be solved with a direct method. The numerical implementation is based on the finite element library `rheolef` [28].

At each time step, we used a mesh adaptive procedure based on a criterion χ related to the flow rate plus a time derivative term:

$$\chi(\hat{t},\hat{x}) = \left(\nu_n\left(\hat{h}, \frac{\partial\hat{h}}{\partial\hat{x}}\right)\left(\frac{\partial\hat{h}}{\partial\hat{x}}\right)^2 + \left(\frac{\partial\hat{h}}{\partial\hat{t}}\right)^2\right)^{1/2}$$

The time derivative term is approximated by the previous second order scheme. The time step is locally optimized for minimizing the local interpolation error χ:

$$\Delta\hat{x}(\hat{t},\hat{x}) = \min\left(\Delta\hat{x}_{\min}^{-2}, \max\left(\Delta\hat{x}_{\max}^{-2}, \left|\frac{\partial^2\chi}{\partial\hat{x}^2}\right|\right)\right)$$

where $\Delta\hat{x}_{\min} = 10^{-4}$ and $\Delta\hat{x}_{\max} = 10^{-1}$. At time t_m, a subdivision is then automatically generated as $\hat{x}_{i+1} = \hat{x}_i + \Delta\hat{x}(\hat{t}_m, \hat{x}_i)$, $i \geq 0$, and $\hat{x}_0 = -1$. As shown on Fig. 2, this procedure is able to capture the front position despite important local gradients and infers the singularity of the solution. The discretization step tends to $\Delta\hat{x}_{\min}$. Conversely, downstream and beyond the front, the solution is zero and the discretization step is $\Delta\hat{x}_{\max}$.

Second order backward difference schemes (BDF2) are well known in the context of stiff systems of ordinary differential equations. Extension to the context of partial differential equations are considered in some rare occasions (see [28] and references herein). Concerning the space discretization, the finite quadratic element polynoms chosen here contrast with the simple afine polynomials used in [29] or [10]. The present numerical scheme provides a fully automatic space-adaptive feature which enables an accurate capture of the front position whereas only a constant space step discretization has been considered in [29, 10]. This one-dimensional adaptive feature is provided by the `Rheolef` finite element library [28].

5. Numerical results and comments

First are presented the numerical results for the case $n = 1$ (i.e. Newtonian fluid).

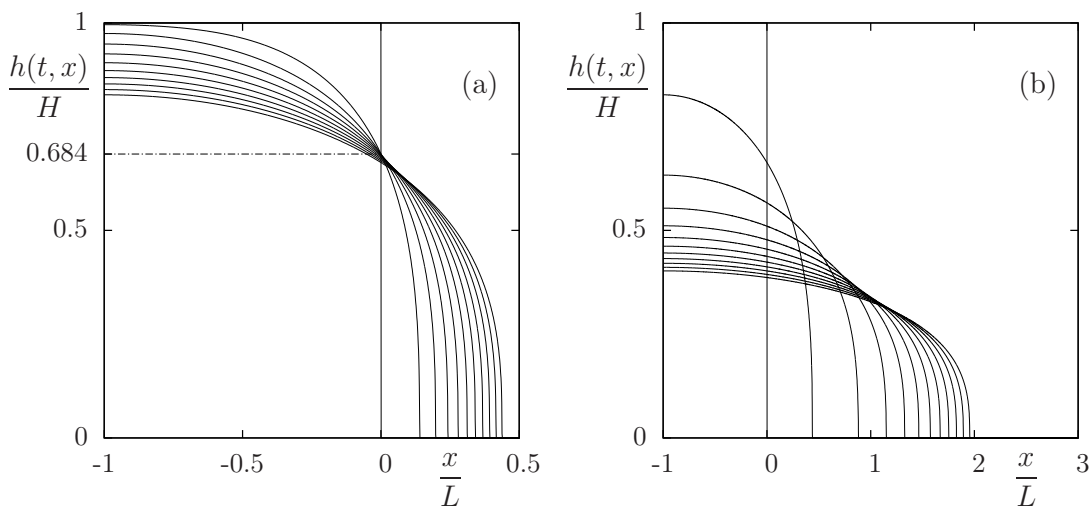

FIGURE 3. Evolution of the free surface for $n = 1$: (a) for small times ($t/T = 0$, 0.24, 0.48, ..., 2.4, from left to right); (b) for medium times ($t/T = 2.4$, 12, 24, ..., 120, from left to right).

5.1. Position of the free surface. For short times, front position and upstream level move rapidly, but at the dam position ($x = 0$) the fluid height remains constant $h(t, x{=}0) \approx 0.684\, H$ (Fig. 3.a). For larger times, when $t > T$, the fluid height starts to decrease significantly at the dam position (Fig. 3.b), while the front position and the free surface in the reservoir move slower. This behaviour is associated with the beginning of a second flow regime. For long times (see Fig. 4.a) the envelope of free surfaces follows a $L/(L + x)$ law while the front position and the flow height in the reservoir show a power-law character. Before going further in the analysis of long-time behaviour, we will discuss first the more classical dam position $h(t, 0)$ at small times.

For $x = 0$ the initial condition $h(t = 0, x)$ is not continuous; the left value is 1 while the right value is zero. Therefore, the exact solution h is also not regular for short times and the convergence becomes difficult in the vicinity of $t = 0$. Fig. 4.b shows the convergence study for $\Delta\hat{t} = 10^{-3}$, 10^{-4} and 10^{-5} while $\Delta\hat{x} = 10^{-4}$. The plot, in logarithmic scale, shows that the fluid height at the dam position tends to

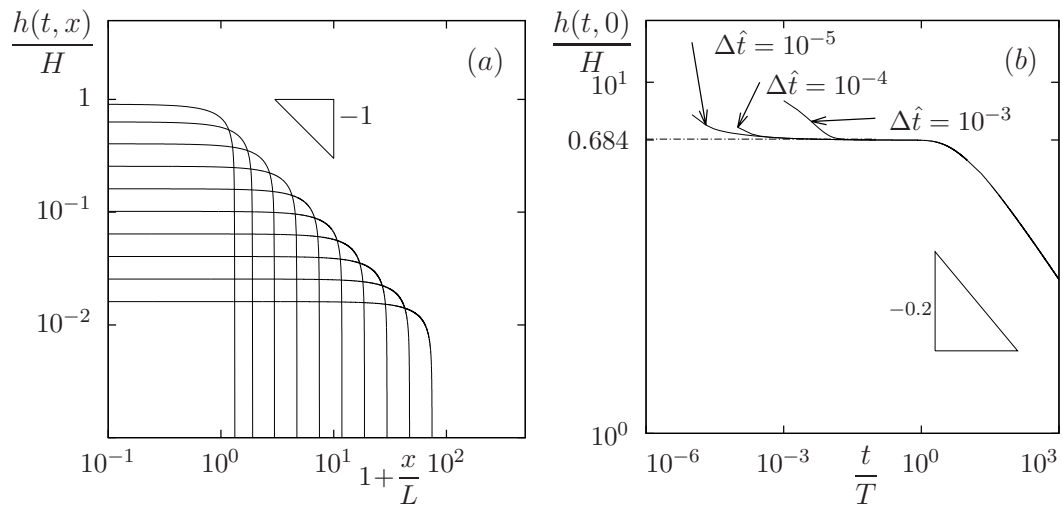

FIGURE 4. Evolution of the free surface when $n = 1$: (a) for large times ($t/T = 1.2$, 1.2×10^1, 1.2×10^2, $\ldots$, 1.2×10^7, from left to right); (b) flow height $h(t, 0)$ at the dam.

remain constant for any arbitrary short time, while the corresponding height is not defined for $(t, x) = (0, 0)$. This result suggests that convergence of $h(t, x=0)$ also occurs when t becomes small, though in a weaker sense than the usual continuous one. In practice, and for all computations in this paper, both the time steps $\Delta\hat{t}$ and element sizes $\Delta\hat{x}$ are automatically adapted. Remark also that $h(t, x=0)$ presents a decreasing power-law behaviour for long times. Fig. 4.b shows the long-time behaviour. The time approximation uses a geometrical progression $t_{m+1} = \alpha\, t_m$ where $\alpha = 10^{0.01}$ in order to match efficiently both short and long-time asymptotic behaviours. This approximation uses 100 time steps per decade. For long times $h(t, x=0)$ behaves as $t^{-1/5}$.

5.2. The front position. Fig. 5.a shows the front position for various values of n. Observe the overall change in slope in the logarithmic scale plot. For short times, $x_f(t)$ behaves as $\sqrt{t}$ while for long times it behaves as $t^{1/5}$. The problem admits two similarity solutions associated to the short- and long-time behaviours [19, 26, 7]. This analysis suggests the following scaling law:

$$\frac{x_f(t)}{L} \approx \begin{cases} 0.284 \left(\dfrac{t}{T}\right)^{1/2} & \text{if } t < 2.5\,T \\[2ex] 1.133 \left(\dfrac{t}{T} + 1.221\right)^{1/5} - 1 & \text{otherwise} \end{cases} \tag{9}$$

The scaling law is not plotted here since there is no further perceptible difference on a graphical representation. More precisely, the relative error is less than 5% and the maximum is always reached in the transition regime while the relative error outside the transition regime is less than 1%. There is a clear advantage of using (9) over classic similarity solutions, which provide only the long-time behaviour. Here, both small-time and long-time behaviours are covered, and the transition regime accuracy is higher than with the direct approaches. Since the purpose of the scaling law is to obtain an easy-to-use formula, (9) will be of great interest for practical

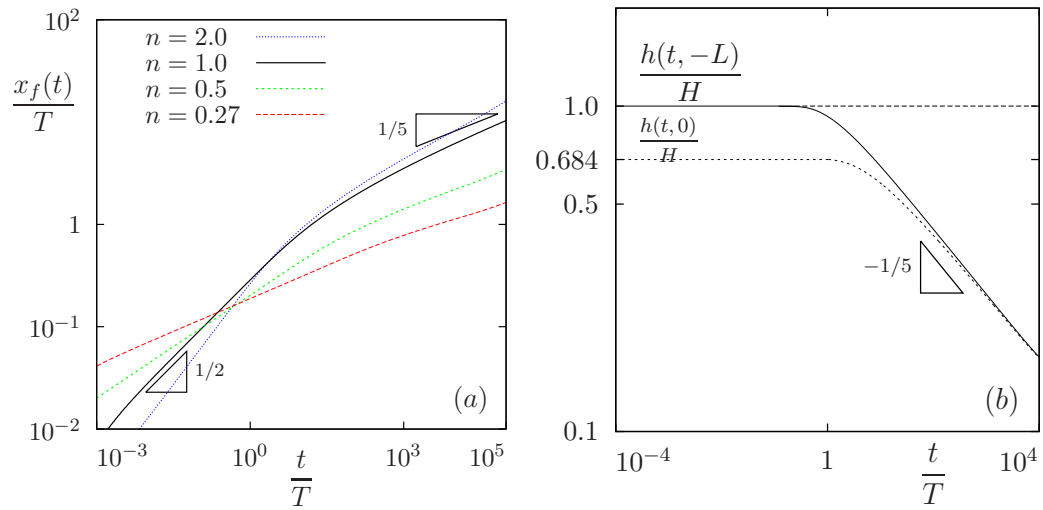

FIGURE 5. (a) Front position $x_f(t)$ for various n; (b) Flow height $h(t, -L)$ in the reservoir when $n = 1$.

applications as no more numerical computations will be required to predict the front position.

The general extension to any $n > 0$ writes:

$$\frac{x_f(t)}{L} \approx \begin{cases} a_n \left(\dfrac{t}{T^*}\right)^{\frac{n}{1+n}}, & \text{when } \dfrac{t}{T^*} < \alpha \\[2ex] b_n \left(\dfrac{t}{T^*} + c_n\right)^{\frac{n}{3+2n}} - 1, & \text{otherwise} \end{cases}$$

where

$$\begin{aligned} a_n &= \frac{1}{3} + 0.944 \left(\frac{n}{1 + 0.548\, n}\right)^{0.85}, \\ b_n &= \left\{ \frac{2(1+n)^{n+4}}{2+n} \left(\frac{3+2n}{n}\right)^n \beta\left(\frac{1}{1+n}, \frac{3+n}{2+n}\right)^{-2-n} \right\}^{\frac{1}{3+2n}}, \\ c_n &= \alpha - \left(\frac{1 + a_n \alpha^{\frac{n}{1+n}}}{b_n}\right)^{\frac{3+2n}{n}}, \\ T^* &= \frac{1+2n}{n}(2+2n)^{\frac{1}{n}} T. \end{aligned}$$

Constant b_n is provided by explicit formula associated to long times flow regime, while a_n is obtained numerically. Here $\beta(.,.)$ denotes the beta function. The continuity between the two flow regimes is enforced at some dimensionless transition time $t/T_* = \alpha$. It requires an appropriate c_n and $\alpha = 2.5$ was used for practical comparisons with direct numerical computations.

5.3. Flow height in the reservoir. Fig. 5.b presents the computation of reservoir height $h(t, x = -1)$ at position $x = -1$ when $n = 1$. For short times, the height at the dam position and the end of the reservoir remain constants (i.e. $h(t, 0)/H = 0.684$ and $h(t, -L) = 1$) while the surface shape rearranges. For long

times, $h(t,-L)$ exhibits a power law $t^{-0.2}$ behavior that matches those of $h(t,0)$. As a result, for long times, the flow height in the reservoir becomes roughly constant versus x and decreases versus time as:

$$\frac{h(t,x)}{H} \approx 0.535 \left(\frac{t}{T}\right)^{-1/5}, \quad -L \leq x \leq 0 \text{ and } t/T_* \gg 2.5$$

A similar behavior is observed for different values of n.

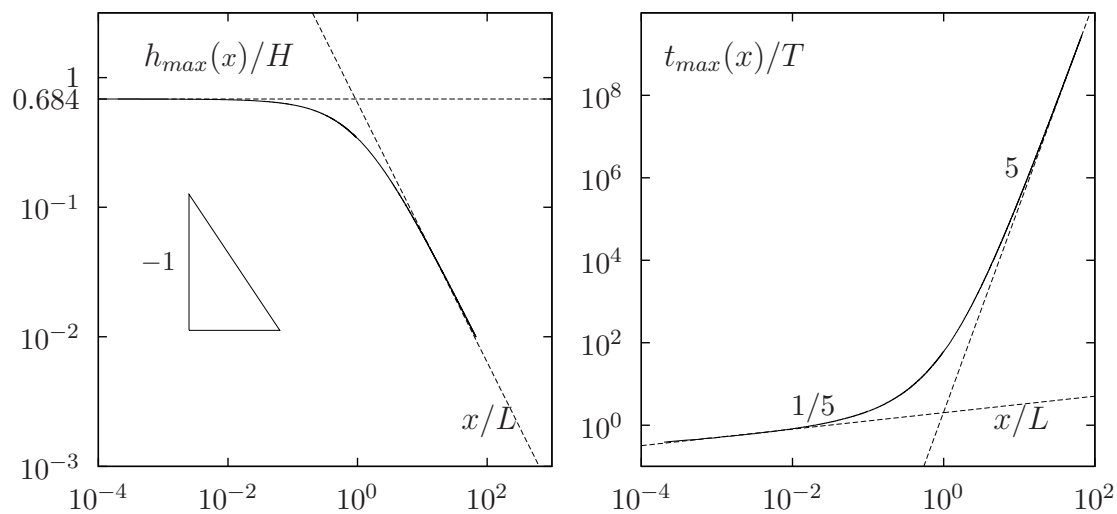

FIGURE 6. When $n = 1$: (a) maximum flow height $h_{max}(x)$; (b) time of maximum flow height $t_{max}(x)$.

5.4. Maximum flow height. For an observer located at $x > 0$, the maximum height denoted by $h_{max}(x)$ is reached at time $t = t^*_{max}(x)$ (see Figs. 6). Observe that, as expected, $h_{max}(x) \approx 0.684\,H$ for small x while $h_{max}(x)$ decreases in $1/x$ for large x, as illustrates the envelope of free surfaces on Fig. 4. All together, it suggests the following scaling law:

$$\frac{h_{max}(x)}{H} \approx 0.684\,\frac{L}{L+x} \tag{10}$$

where the coefficients are provided by a non-linear least-square fitting.

Once the maximum flow height is reached, the time behaves as x^5 for large x and $x^{1/5}$ for small x and the time of the peak streamflow may express as:

$$t_{max}(x) \approx 2\left(\frac{x}{L}\right)^{1/5} + 2.1\left\{\left(\frac{L+x}{L}\right)^5 - 1\right\} \tag{11}$$

6. Comparisons with experiments

We opposed our theoretical findings to some experiments performed with silicon. In the first paragraph we present the experimental setup while this section ends with the comparison between theory and both experiments for silicon and previous measurements available in the literature for other various materials.

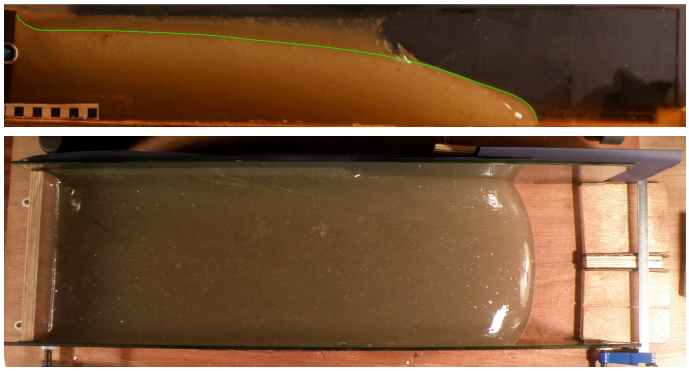

FIGURE 7. Experimental set-up: (a) face view, where the red line indicates the free surface as generated by image processing; (b) top view.

6.1. Experimental set-up. We used a transparent synthetic polymer SGM 36. Made by Dow Corming (USA), SGM 36 is the industrial code of a polymer liquid between 200 and 550 K. It consists in linear polydimethylsiloxane molecules. In the presented flow conditions, this material can be considered as a Newtonian fluid and its viscosity is 4×10^4 Pa s at room temperature [30]. We used an horizontal channel (see Fig. 7.a) of width W, confined between two plates of Plexiglas, with a reservoir of length L and height H. Fig. 7.b shows that the flow front is relatively flat, suggesting that the slump is largely two-dimensional and the side walls do not have much effect. (see also Fig. 6 in [7] or Fig. 8 in [26] for similar considerations). Slip at the side walls is enforced with a penetrating grease but the fluid sticks at the wood bottom boundary. Both widths $W = 115$ mm and 225 mm have been tested in order to check that tridimensional effects are negligible and that measurements are independent of the width W. Both reservoir lengths $L = 160$ mm and 320 mm have been tested. In all experiments the initial flow height $H = 115$ mm remains constant. Digital photography of the front view are performed with a period of 20 seconds. Using an image processing tool, we are able to extract the flow profiles and the successive front positions x_f.

6.2. Comparisons. We note that in the numerical simulations of the dam-break problem the whole bulk of fluid was assumed to be released instantaneously, i.e. the time needed for the gate to open was neglected. In the experimental apparatus, the removal of the gate is gradual. It starts to move at $t = 0$ and is completely raised after a non negligible time. In our modelling, the time to fully open the gate can be interpreted as a delay $t = t_0$. Since this delay is not known, it should be adjusted with experimental measurements for a non distorted comparison.

Most experimental results was obtained for Newtonian fluids ($n = 1$), while very few measurements are available for non-Newtonian power-law fluids. Figs. 8.a to 8.c confirm that our computations compare well with various measurements on Newtonian fluids, as obtained by others authors or by us (Fig. 8.c). Fig. 8.a compares our prediction with measurements obtained with some corn sirup [7, Fig. 7.a]. Fig. 8.b compares also with a glucose solution [26]. For both materials a good concordance exists between predictions and measurements. The small time flow regime on Fig. 8.b develops a slope of one suggesting a first inertia flow regime. However, the comparison with the corresponding Ritter solution $x_f = (gH)^{\frac{1}{2}} t$ is

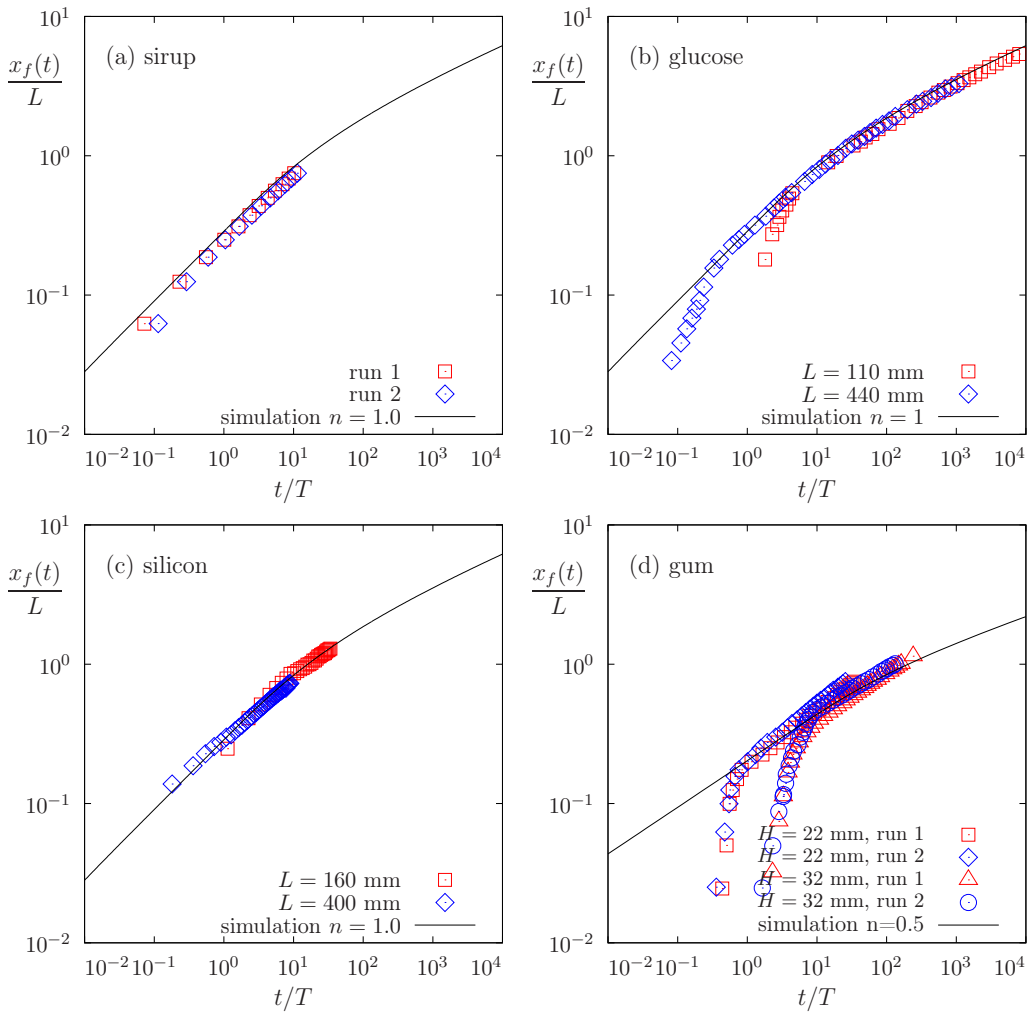

FIGURE 8. Front position: comparison between experimental measurements and theoretical predictions with (a) corn sirup [7, Fig 7.a] ; (b) glucose [26] ; (c) silicon ; (d) gum [7, Fig 9.b].

not satisfactory and such a slope is better explained by the lifting of the dam. The complete set of flow and material parameters used for all the comparison in this paragraph are summarised in table 1. Fig. 8.c shows the comparisons with our present measurements on silicon. Fig. 8.d compares with the only one measurement available to our knowledge for a power-law fluid on the dam break problem: it is a xantham gum [7, Fig 9.b] associated with a power-law index $n = 0.5$. Likewise the Newtonian case the small time flow regime is not related to inertia effects and could be due to the lifting of the dam.

Let us come back to the present measurements on silicon. Fig. 9 shows the free surface profiles for the two reservoir lengths with the same height $H = 11.5$ cm and width $W = 22.5$ cm. The profiles are globally in good concordance with some small discrepancies. The theory predicts a lower profile at upstream and a higher one at

	$L(cm)$	$H(cm)$	$\rho(g/cm^3)$	n	$K(m.k.s)$
sirup	40	2.2	1.40	1.0	4
glucose	11, 44	5.5	1.40	1.0	12
silicon	16, 40	11.5	1.40	1.0	40 000
gum	40	2.2, 3.2	1.00	0.5	7.5

TABLE 1. Flow and material parameters used for the comparisons.

downstream. A possible explanation of this discrepancies could be the development of localised viscoelastic effects in the front region, where shear rates are higher.

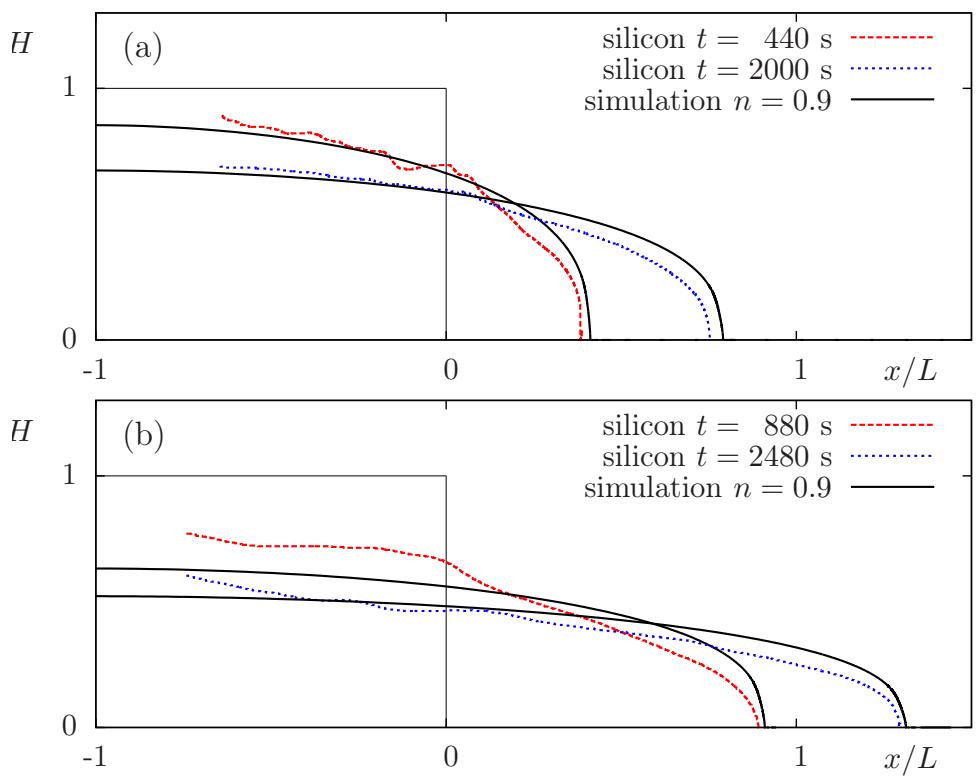

FIGURE 9. Free surface : comparison between theoretical prediction with $n = 0.9$ and experimental measurements with silicon when $H = 115mm$ and $W = 225mm$: (a) $L = 440mm$, and (b) $L = 160mm$.

7. Conclusion

Using silicon, this paper appends new measurements of the non-Newtonian power-law case for the horizontal dam break problem. Based on a new time-space second-order adaptive algorithm, the shallow approximation of the problem has been solved and solutions compared with both silicon and other measurements for Newtonian and non-Newtonian materials. These comparisons confirm the validity of the slow flow shallow approximation equations for the horizontal dam break

problem for these materials. The numerical resolution of this nonlinear problem point out difficulties associated to two kinds of sharp transitions. The first sharp transition is related to variation in time, at the vicinity of $t = 0$. In order to handle this transition, an implicit second order time approximation and a varying time step adaptation is developed. A second sharp transition is related to space, at the vicinity of the front position $x = x_f(t)$, where a second order polynomial approximation and an automatic space-mesh adaptation is developed. Finally the adaptive numerical algorithm is seen as a good candidate to handle three-dimensional free surface flows on complex topographies. Actually under development, this last improvement may find practical interests for geophysical flows such as mud or volcanic lava flows.

References

[1] R. A. Adams and J. J. F. Fournier. *Sobolev spaces*. Elsevier, second edition, 2003.

[2] C. Ancey. *Snow avalanches*, pages 319–338. Springer, 2001.

[3] C. Ancey. Plasticity and geophysical flows: a review. *J. Non-Newtonian Fluid Mech.*, 142 (2007) 4–35.

[4] C. Ancey and S. Cochard. The dam-break problem for Herschel-Bulkley viscoplastic fluids down steep flumes. *J. Non-Newtonian Fluid Mech.*, 158 (2009) 18–35.

[5] C. Ancey, S. Cochard, and N. Andreini. The dam-break problem for viscous fluids in the high-capillary-number limit. *J. Fluid Mech.*, 624 (2009) 1–22.

[6] N. J. Balmforth and R. V. Craster. A consistent thin-layer theory for Bingham plastics. *J. Non-Newtonian Fluid Mech.*, 84 (1999)(1) 65–81.

[7] N. J. Balmforth, R. V. Craster, P. Perona, A. C. Rust, and R. Sassi. Viscoplastic dam breaks and the Bostwick consistometer. *J. Non-Newtonian Fluid Mech.*, 142 (2007)(1–3) 63–78.

[8] N. J. Balmforth, R. V. Craster, A. C. Rust, and R. Sassi. Viscoplastic flow over an inclined surface. *J. Non-Newtonian Fluid Mech.*, 139 (2006) 103–127.

[9] E. C. Bingham. *Fluidity and plasticity*. Mc Graw-Hill, 1922.

[10] J. G. Blom and P. A. Zegeling. Algorithm 731: a moving-grid interface for systems of one-dimensional time-dependent partial differential equations. *ACM Transactions on Mathematical Software (TOMS)*, 20 (1994)(2).

[11] P. Coussot. Steady, laminar, flow of concentrated mud suspensions in open channel. *J. Hydr. Res.*, 32 (1994)(4) 535–559.

[12] M. Fortin and R. Glowinski. *Augmented Lagrangian methods*. Elsevier, 1983.

[13] J.-F. Gerbeau and B. Perthame. Derivation of viscous Saint-Venant system for laminar shallow water; numerical validation. *Discrete and continuous dynamical systems - serie B*, 1 (2001)(1) 89–102.

[14] R. W. Griffiths. The dynamics of lava flows. *Annual Review of Fluid Mechanics*, 32 (2000) 477–518.

[15] M. A. Hampton, H. J. Lee, and J. Locat. Submarine landslides. *Reviews of geophysics*, 34 (1996)(1) 33–59.

[16] W. H. Herschel and T. Bulkley. Measurement of consistency as applied to rubber-benzene solutions. *Am. Soc. Test Proc.*, 26 (1926)(2) 621–633.

[17] A. J. Hogg and D. Pritchard. The effects of hydraulic resistance on dam-break and other shallow inertial flows. *J. Fluid Mech.*, 501 (2004) 179–212.

[18] X. Huang and M. Garcia. A Herschel-Bulkley model for mud flow down a slope. *J. Fluid Mech.*, 374 (1998) 305–333.

[19] H. E. Hupper. The propagation of two-dimensional and axisymmetric viscous gravity currents over a rigid horizontal surface. *J. Fluid Mech.*, 121 (1982) 43–58.

[20] D. Laigle and P. Coussot. Numerical modeling of mudflows. *J. Hydr. Engrg.*, 123 (1997)(7) 617–623.

[21] K. F. Liu and C. C. Mei. Approximate equations for the slow spreading of a thin sheet of a Bingham plastic fluid. *Phys. Fluids A*, 2 (1990) 30–36.

[22] R. R. Milczarek and K. L. McCarthy. Relationship between the Bostwick measurement and fluid properties. *J. Texture Studies*, 37 (2006)(6) 640–654.

[23] R. Perona. Bostwick degree and rheological properties: an up-to-date viewpoint. *Appl. Rheol.*, 15 (2005)(4) 218–229.

[24] J.-M. Piau. Consistometry slump and spreading tests: Practical comments. *J. Non-Newtonian Fluid Mech.*, 135 (2006) 177–178.

[25] J.-M. Piau and K. Debiane. The adhesive or slippery flat plate viscoplastic boundary layer for a shear-thinning power-law viscosity. *J. Non-Newtonian Fluid Mech.*, 117 (2004) 97–107.

[26] J.-M. Piau and K. Debiane. Consistometers rheometry of power-law viscous fluids. *J. Non-Newtonian Fluid Mech.*, 127 (2005) 213–224.

[27] A. J. C. Barré de Saint-Venant. Théorie et équations générales du mouvement non permanent des eaux courantes. *Comptes Rendus des séances de l'Académie des Sciences, Paris, France, Séance 17*, 73 (1871) 147–154.

[28] P. Saramito. *Efficient C++ finite element computing with Rheolef*. CNRS and LJK, 2011. http://www-ljk.imag.fr/membres/Pierre.Saramito/rheolef.

[29] R. D. Skeel and M. Berzins. A method for the spatial discretization of parabolic equations in one space variable. *SIAM journal on scientific and statistical computing*, 11 (1990)(1) 1–32.

[30] R. Weijermars. Finite strain of laminar flows can be visualized in SGM36-polymer. *Naturwissenschaften*, 73 (1986)(1) 33–34.

[1] Lab. J. Kuntzmann – CNRS and Grenoble university, B.P. 53, 38041 Grenoble cedex 9, France

[2] Lab. géosciences – IPGP and La Réunion university, 15, av. René Cassin, CS 92003, 97744 Saint-Denis cedex 09, France

[3] Earth and Planetary Science, UC Berkeley, Mc Cone Hall, Berkeley CA 94720-4767, USA

E-mail: pierre.saramito@imag.fr and claude.smutek@univ-reunion.fr and benoit.cordonnier@erdw.ethz.ch

URL: http://www-ljk.imag.fr/membres/Pierre.Saramito